

A Direct Detection of Dust in the Outer Disks of Nearby Galaxies

Amy E. Nelson

Board of Astronomy and Astrophysics, Univ. of California, Santa Cruz, CA, 95064,

E-Mail: anelson@ucolick.org

Dennis Zaritsky

UCO/Lick Observatory and Board of Astronomy and Astrophysics, Univ. of California,

Santa Cruz, CA, 95064, E-Mail: dennis@ucolick.org

and

Roc M. Cutri

IPAC-Caltech, Mail Stop 100-22, Pasadena, CA, 91125, E-Mail: roc@ipac.caltech.edu

ABSTRACT

We measure the extent of $100\mu\text{m}$ galactic emission in two independent galaxy samples using the IRAS $100\mu\text{m}$ Sky Survey images and constrain the distribution of dust at large ($\lesssim 30$ kpc) radii. The first sample consists of 90 nearby ($v < 6000$ km/s) galaxies from the RC3 catalog with similar angular sizes and absolute luminosities ($5' \leq D_{25} \leq 10'$ and $-22.5 \leq M_B \leq -18$) that are isolated in the $100\mu\text{m}$ images. The second sample consists of 24 local galaxies ($v < 1500$ km/s, $10' \leq D_{25} \leq 30'$). We rescale the $100\mu\text{m}$ images of these galaxies using their optical diameters, D_{25} , rotate the images using their optical major axis position angle, construct the mean and median image, and rebin the final images into polar coordinates to study the $100\mu\text{m}$ emission as a function of radius and azimuthal angle. We find that the $100\mu\text{m}$ emission extends at least to radii of 27 kpc (2σ detection) for the typical galaxy in the $5' - 10'$ sample and to 21 kpc (2σ detection) in the $10' - 30'$ sample ($H_0 = 75$ km/s/Mpc). In both samples, the emission is preferentially elongated along the optical major axis. We fit an exponential to the $100\mu\text{m}$ emission along the major axis and measure a scale length of 2.5 ± 0.8 kpc (90% confidence interval). Using a simple model that relates the far-IR emission to the stellar distribution, we examine the range of acceptable dust mass distributions allowed by our data and conclude that the dust is more extended than the starlight.

Subject headings: dust,extinction — galaxies: ISM — galaxies: spiral
— infrared radiation — surveys: IRAS

1. Introduction

Of the three principal baryonic components of any galaxy – stars, gas, and dust – the distribution of dust is the least understood. The radial density distribution of the stellar component in disk galaxies falls off exponentially with a scale length ranging from $\sim 1 - 10$ kpc (de Jong 1996a, 1996c) out to an abrupt radial cutoff (van der Kruit and Searle 1981a, 1981b, 1982a, 1982b). The radial density distribution of neutral hydrogen is flat (e.g. Shaya and Federman 1987) out to a radial cutoff, while that of molecular gas is generally exponentially decreasing (e.g. Young and Scoville 1991) even though there is evidence for the presence of cold molecular gas at large galactic radii (e.g. Lequeux *et al.* 1993; Fich *et al.* 1989; Wouterloot *et al.* 1990). These various distributions have been used to study the formation of disks (cf. Fall & Efstathiou 1980; Lin & Pringle 1987), star formation in disks (Kennicutt 1989), and the relation between the neutral hydrogen fraction and the ionizing intergalactic radiation field (Maloney 1993). Does dust trace the stellar or gaseous components (either the atomic or molecular phase)? The resolution of this question may yield insight into past star formation in galactic disks and into the energetics and transport of the interstellar medium throughout disks. The goal of this study is to infer the average radial and angular distribution of dust at large radii in galaxies, by measuring the $100\mu\text{m}$ emission from ensembles of galaxies.

Existing studies of dust in galaxies rely on one of two physical phenomena: (1) the extinction of light by dust grains (e.g. Zaritsky 1994; Block *et al.* 1994; Peletier *et al.* 1995; de Jong 1996b); and (2) the emission of FIR/mm light by dust grains (e.g. Rice *et al.* 1988; Bothun & Rogers 1992; Andreani & Franceschini 1996; Odenwald, Newmark & Smoot 1996). The application of either approach becomes increasingly difficult at larger radii. By measuring the extinction of background galaxies observed through the halos of two large, nearby spirals, Zaritsky (1994) presented preliminary evidence of dust at radii of ~ 60 kpc. Studies of the far-IR emission from galaxies have focused on dust within the optically luminous disks of nearby galaxies of large angular extent (Rice *et al.* 1988; Bothun, Lonsdale, Rice 1989; Bothun & Rogers 1992; Rice 1993). Bothun and Rogers (1992) detected $100\mu\text{m}$ emission out to approximately 30 kpc in 6 of the 28 galaxies in their sample. However, the signal-to-noise is rather low in these outer regions, and there is limited spatial information. Reliable, general constraints on the distribution of dust beyond ~ 15 kpc are scarce.

We strive for sensitivity by coadding the $100\mu\text{m}$ images of 115 galaxies drawn

from the IRAS Sky Survey Atlas (ISSA; Wheelock *et al.* 1994) to measure the radial extent, profile, and azimuthal distribution of the thermal dust emission. We choose to work with the longest wavelength IRAS images because we are interested in the distribution of dust at large radii, which is most likely cold ($\lesssim 30K$) and therefore has peak emission at $\lambda \gtrsim 100\mu\text{m}$. In §2, we discuss the selection criteria for the sample and control galaxies, and describe our algorithm. In §3, we present the results obtained from the two samples. Finally, in §4, we model the $100\mu\text{m}$ emission, and present a simple model which constrains the dust distribution.

2. The Data

2.1. Sample Selection

Our measurement of the emission from cold dust in galaxies is based on the combination of $100\mu\text{m}$ ISSA images (Wheelock *et al.* 1994) and basic galactic data from the Third Reference Catalog of Bright Galaxies (RC3; de Vaucouleurs *et al.* 1991). We limit our study to Galactic latitudes $b \gtrsim 15^\circ$ and $b \lesssim -40^\circ$ to minimize Galactic cirrus contamination and select candidates from the RC3 based solely on their coordinate positions, regardless of other galactic properties such as morphology. Figure 1 shows a $\sim 20^\circ \times 20^\circ$ section of the $100\mu\text{m}$ Atlas near $(\alpha, \delta) = (1^h 20^m, 0^\circ)$ or equivalently $(l, b) = (139.5^\circ, -61.6^\circ)$. The images have $1.5'$ pixels. The filamentary features of large angular extent are due to Galactic cirrus (Low *et al.* 1984). The numerous small, high surface brightness knots are predominantly galaxies and are typically comparable in size to the point spread function of the survey (FWHM $\simeq 5'$; ISSA Explanatory Supplement).

The most serious difficulty faced by this study is the irregular structure of the Galactic foreground emission. As illustrated in Figure 1, the contamination can be high even at high galactic latitude. To ensure that the final sample of galaxies do not have close companions and that they lie in quiescent regions of the foreground sky, we identify each candidate on the ISSA images using the RC3 coordinates and a gnomonic coordinate projection centered on the central coordinates of our 35° survey images, and apply the following criteria:

(1) *Centering Convergence* : The galaxies' $100\mu\text{m}$ luminosity centroids are calculated using the IRAF CENTER routine¹. We reject galaxies with $100\mu\text{m}$

¹IRAF is distributed by the National Optical Astronomical Observatories, which are operated by AURA,

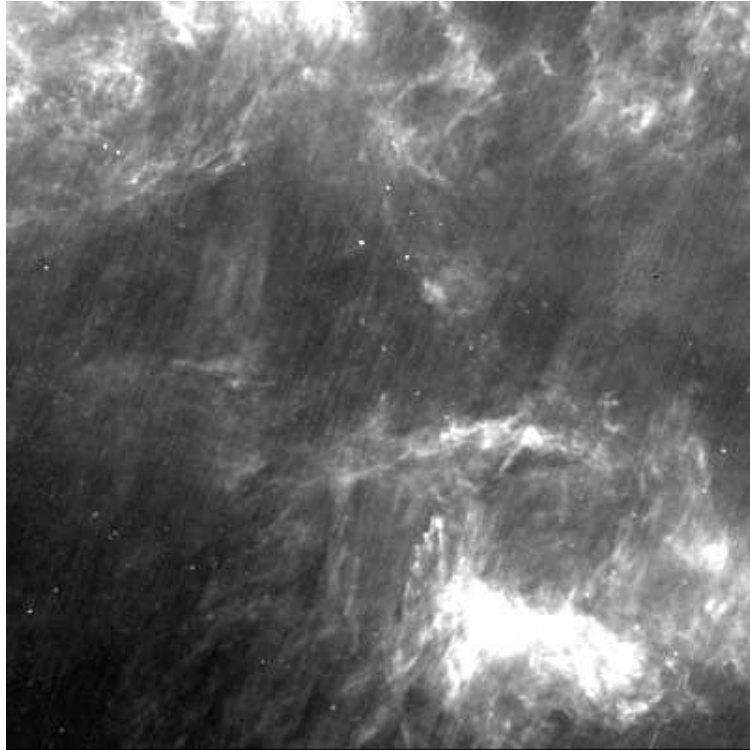


Fig. 1.— A $\sim 20^\circ \times 20^\circ$ section of the ISSA Atlas near $(\alpha, \delta) = (1^h 20^m, 0^\circ)$ or equivalently $(l, b) = (139.5^\circ, -61.6^\circ)$. The filamentary features of large angular extent are due to Galactic cirrus, while the numerous small higher surface brightness knots are predominantly galaxies.

centroids that have internal uncertainties $>0.45'$ in either x or y ($> 1/3$ of a pixel), or that have $100\mu\text{m}$ centroids that differ by more than $2.25'$ ($\sim 0.5 \times \text{FWHM}$ of a point source) from the projected coordinates. Typically, galaxies fail these criteria if they have low signal-to-noise, a close companion, or lie in regions of high cirrus contamination. About 90% of the original 23660 possible target galaxies are rejected due to this criteria.

(2) *Photometric Convergence* : We perform aperture photometry on the remaining galaxy candidates using the IRAF PHOT routine and apertures with radii from $1.5'$ to $10.5'$ spaced by $1.5'$. We reject any galaxy whose magnitude does not converge on the grounds that the local background must be strongly affected by cirrus emission. This step excludes $\sim 6\%$ of the remaining targets.

(3) *Image Edge and Bad Pixel Contamination* : Galaxies within $52.5'$ (a distance equal to the region of the extracted subimage used in the analysis) of the image edge are rejected. In addition, the process of mosaicing smaller images to produce the $\sim 30^\circ \times 30^\circ$ ISSA images can create streaks of bad pixels at the interface of the sub-images. Any galaxies falling in regions of these bad pixel streaks are rejected. Because both the shape of the final mosaic images and the initial sub-images vary from image to image, this step is done interactively and excludes $\sim 17\%$ of the remaining galaxies.

(4) *Multiple Identifications* : Any $100\mu\text{m}$ source that was associated with multiple optical sources was rejected; excluding $\sim 9\%$ of the remaining galaxies.

(5) *Close Companion Contamination* : To avoid contamination from close companion galaxies, we reject any galaxy with a cataloged companion within $30'$ projected separation. This cut excludes $\sim 20\%$ of the remaining targets.

(6) *Visual Inspection* : To ensure that the final galaxy sample is not contaminated by either strong cirrus or close companions not listed in the RC3, we visually inspected each image. Interactively, we only removed 3% of the remaining galaxies. Overall, 95% of the original galaxies are rejected due to the above cuts.

This procedure yields a heterogeneous set of isolated galaxies, which span a wide range of sizes, distances, luminosities, and inclinations. For the addition of galaxy images to be physically meaningful, we must normalize their apparent angular scales and brightness using their isophotal diameters and their central surface brightnesses. In defining the final samples, we want to maximize the number of galaxies to increase the sensitivity yet minimize the range of

isophotal diameters and central surface brightness to avoid large scaling factors that greatly magnify the point spread function, PSF, (which could mask an otherwise resolvable detection) and decrease the signal-to-noise ratio. Therefore, we impose two conditions. First, the isophotal diameters of galaxies in any particular sample cannot be scaled by more than a factor of three. We bin the samples into three groups according to D_{25} : $2.5' - 5'$, $5' - 10'$, and $10' - 30'$. Second, the galaxies must be within a limited range of intrinsic luminosities. We include those galaxies in the $2.5' - 5'$ and $5' - 10'$ samples that have $-18 > M_B > -23$ ($H_0 = 75$ km/s/Mpc in all calculations). The galaxies in the $10' - 30'$ sample are sufficiently nearby that calculating luminosities using recessional velocities, V_{rad} , is not accurate ($\langle V_{rad} \rangle = 748$ km/s), so no luminosity cuts are made.

The final samples consist of 24 galaxies in the $10' - 30'$ sample, 91 galaxies in the $5' - 10'$ sample, and 184 galaxies in the $2.5' - 5'$ sample. The distributions of recessional velocities, R_{25} , and M_B for each sample, if available, are shown in Figures 2, 3, 4. A summary of the mean properties of each sample is given in Table 1. Although no selection criteria were imposed regarding galaxy type, the samples are predominantly galaxies classified as type Sd to Sa in the RC3, as shown in Figure 5. This is an indirect result of selecting galaxies from the $100\mu\text{m}$ images, a spectral regime where emission from dusty late-type galaxies dominates over the relatively dust-free early-type galaxies. Notice that the galaxies in the $10' - 30'$ and $5' - 10'$ samples appear to contain nearly identical galaxies because they both have $\langle R_{25} \rangle \sim 18.5$ kpc, while the $2.5' - 5'$ sample appears to be dominated by galaxies that are physically smaller, $\langle R_{25} \rangle \sim 13.5$ kpc. Finally, as we discuss below, we take care to select a control sample with the same quantitative criteria as used to select the original

Table 1. Sample Properties

Sample	Number	D_{25}	V_{rad} (km/s)	$\langle V_{rad} \rangle$ (km/s)	M_B (mag)	$\langle R_{25} \rangle$ (kpc)
$10' - 30'$	24	$10' - 30'$	0 – 1600	750	...	18.9
$5' - 10'$	91	$5' - 10'$	500 – 3300	1500	–18 to –23	18.1
$2.5' - 5'$	184	$2.5' - 5'$	700 – 6800	2100	–18 to –23	13.6
Control Galaxies	200	$0' - 1.5'$	1000 – 16000	5800	–18 to –23	...
Control Stars	30

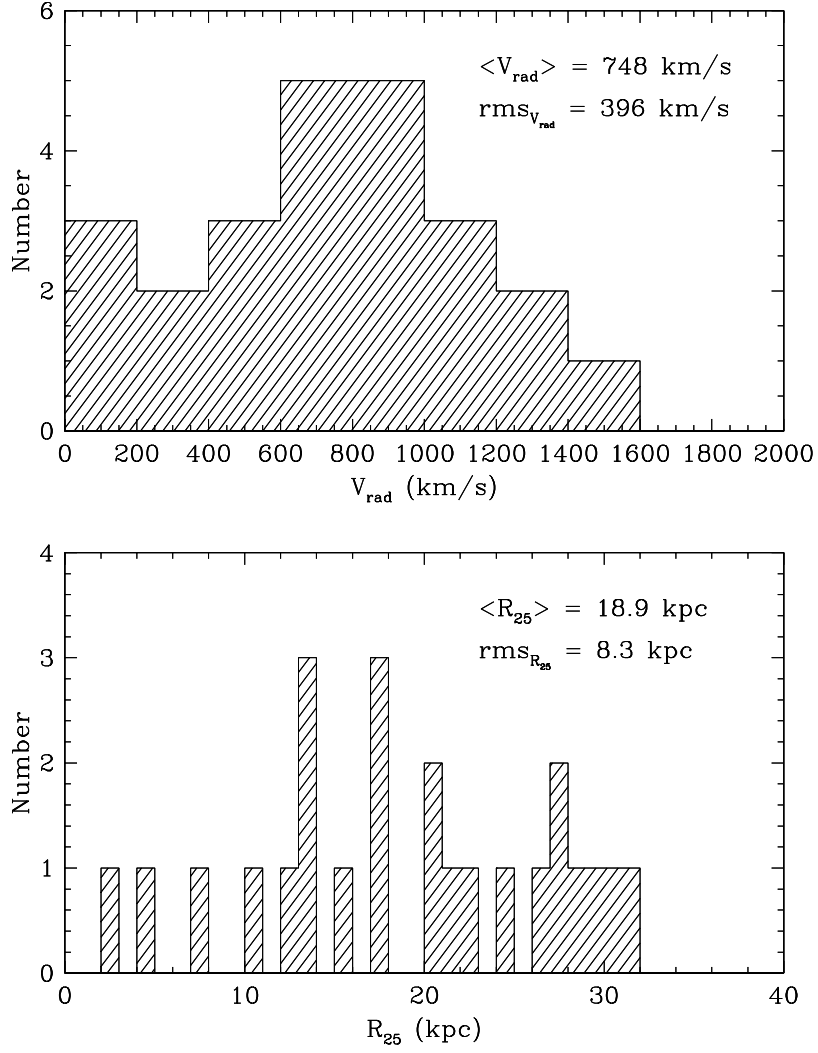


Fig. 2.— The distributions of recessional velocities and R_{25} for the $10' - 30'$ sample of 24 galaxies.

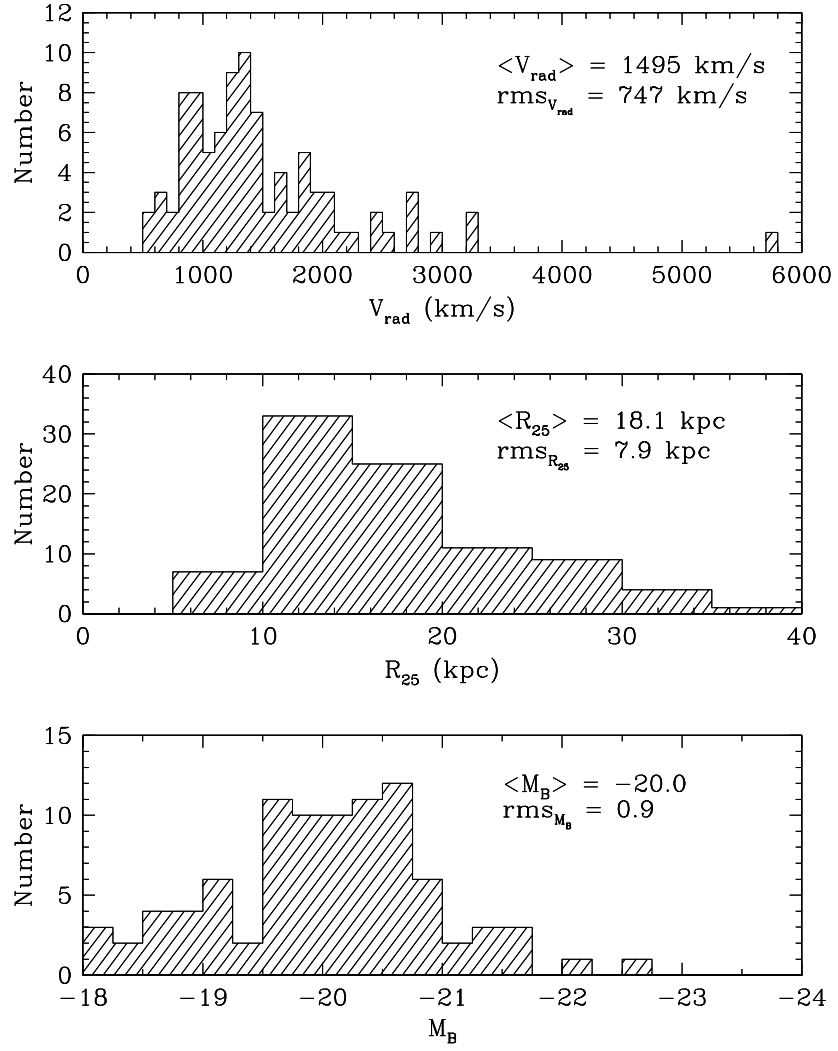


Fig. 3.— The distributions of recessional velocities, R_{25} , and M_B for the $5' - 10'$ sample of 91 galaxies.

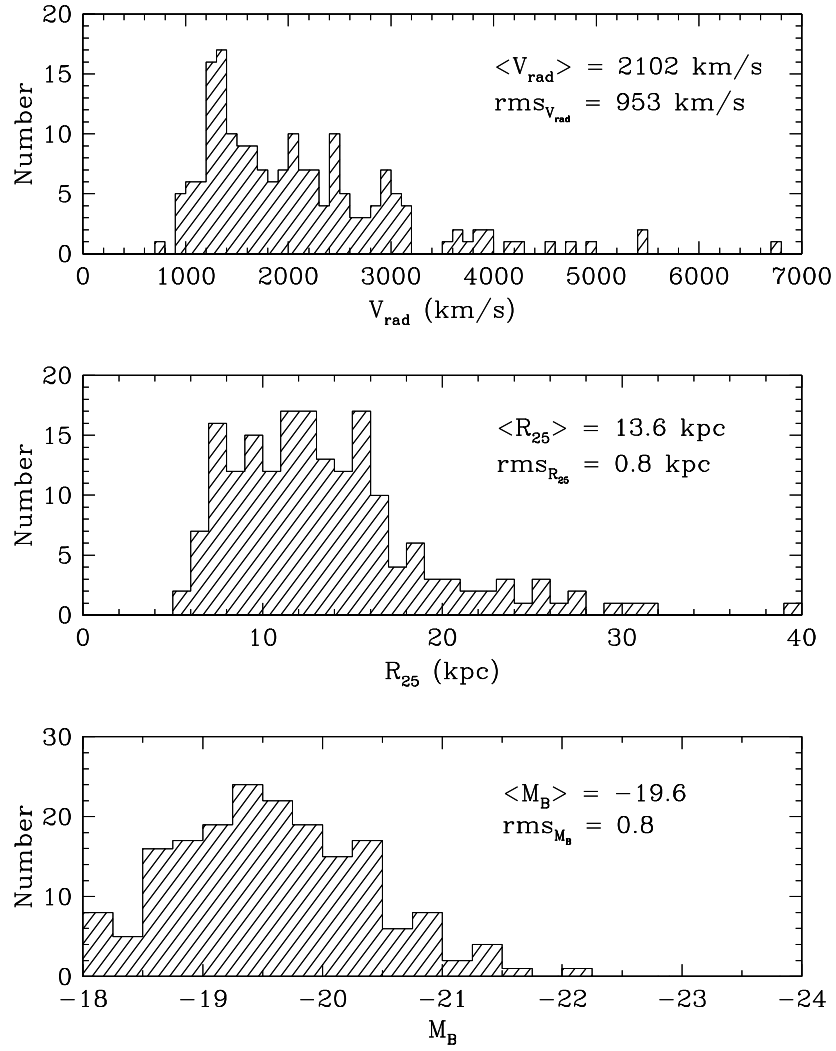


Fig. 4.— The distributions of recessional velocities, R_{25} , and M_B for the $2.5' - 5'$ sample of 184 galaxies.

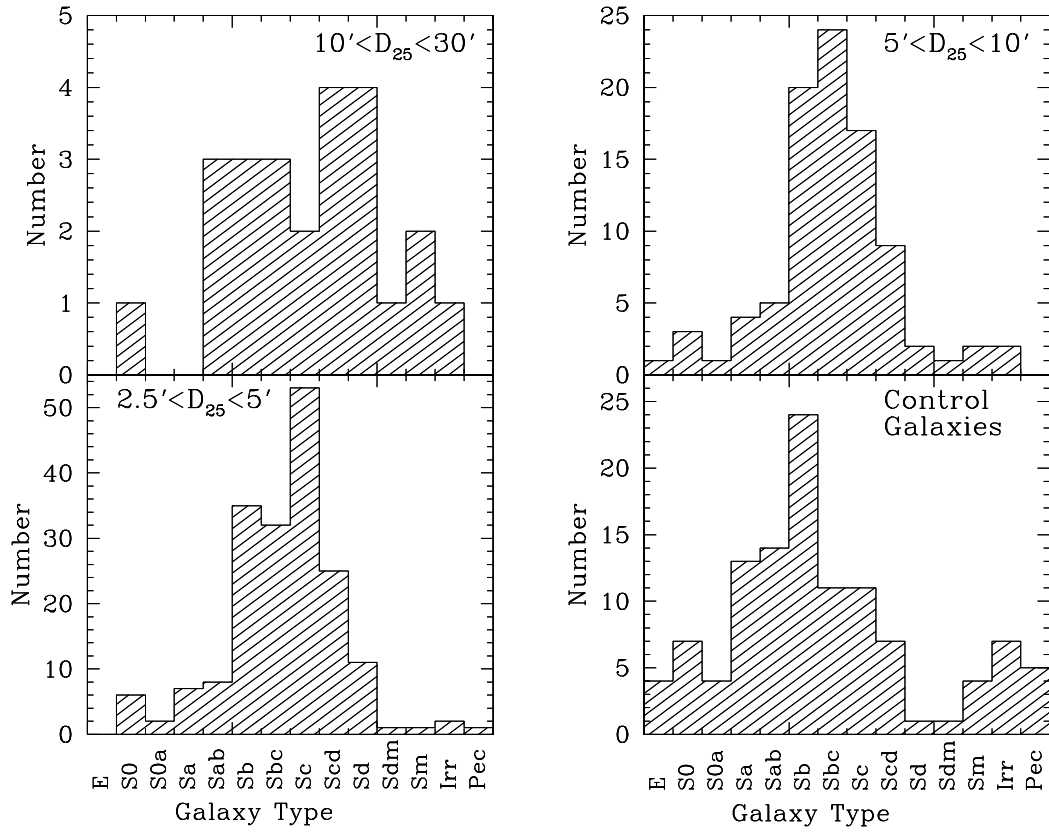


Fig. 5.— The distribution of galaxy type, as listed in the RC3, for all three samples of galaxies and the control galaxies.

samples.

2.2. Coadded Images and the Point Spread Function

The exact procedure we use to prepare the galaxy images to be coadded consists of the following steps:

- (1) we extract a subimage of $121.5' \times 121.5'$ (81 pixels) centered on each galaxy using the $100\mu\text{m}$ galaxy centroid;
- (2) this subimage is rotated and scaled using IRAF’s IMLINTRAN routine and the optical position angle and D_{25} from the RC3, while conserving total flux;
- (3) we subtract a mean sky value measured in an annulus defined by $30' < R < 52.5'$, where R is the radius from the target galaxy; and
- (4) we normalize the flux, as measured by our aperture photometry, so that the galaxy’s central surface brightness is equal to unity.

Upon completion, the resulting images of each galaxy are combined into a mean and median image, applying 10σ clipping to remove spurious pixels. The outer border (width = 10 pixels) of the resulting co-added image is fit by a plane to remove any large scale sky variations. The image is then rebinned into polar coordinates, which allows a straightforward comparison of the radial extent of the $100\mu\text{m}$ emission as a function of polar angle (e.g. Fig 7). Finally, the sky is resubtracted (always a small subtraction, $< 1\%$) and the central surface brightness is renormalized (always a small division factor, resulting in $< 1\%$ effect). The result of this procedure is an image in polar coordinates that is the sum of 184 galaxies in the $2.5' - 5'$ sample, 91 galaxies in the $5' - 10'$ sample, and 24 galaxies in the $10' - 30'$ sample from which we measure the shape and extent of the $100\mu\text{m}$ emission.

We do not attempt any correction for galaxy inclination angle. For all but the most nearby, face-on galaxies, the $5'$ PSF of the ISSA images equals or exceeds the galaxies’ minor axes. However, the major difficulty with any attempt at deprojection is the complex background component that cannot be removed on a galaxy-by-galaxy basis. The other option to address this issue, exclusion of lower inclination galaxies, is also not tenable. This option substantially decreases the sample size and our ability to detect emission at large radii. Therefore, we have chosen to apply no inclination correction, but only present quantitative results from data taken along the major axis of the final summed image, which is least affected by inclination.

Most, if not all, of the $100\mu\text{m}$ emission from galaxies in the samples are dominated by emission from the unresolved or marginally resolved inner portions

of the disks. Consequently, our ability to detect extended $100\mu\text{m}$ emission is highly dependent on the determination of an accurate $100\mu\text{m}$ point spread function. At a distance of 25 Mpc, $\langle D_{25} \rangle$ corresponds to $5'$. The IRAS $100\mu\text{m}$ PSF is $\sim 5'$ on the longest side, but is asymmetric and varies spatially across the images because of survey coverages and thus, is too complicated to model. We will rely on an empirical determination from two independent sets of unresolved sources.

To determine the point spread function in an empirical manner that is entirely consistent with the collection and analysis of our sample, we select two independent sets of unresolved sources: stars detected in all four bands in the IRAS Faint Source Catalog; and compact galaxies ($D_{25} \leq 1.5'$) from the RC3 catalog. As long as stars do not have extended structure (such as debris disks or envelopes) then they are truly point sources, and so, apparently an ideal control set to determine the PSF empirically. Such extended structure is characterized by an IR excess, and therefore we select stars with $F_{12} > F_{60}$, where F_{12} and F_{60} are the fluxes at $12\mu\text{m}$ and $60\mu\text{m}$, respectively. Unfortunately, there are too few stars (30 that survived our selection criteria) to compare to the more numerous $2.5' - 5'$ and $5' - 10'$ samples, and the stars have a much higher central surface brightness than the galaxies, which may be an issue with detector hysteresis. However, because the $10' - 30'$ sample is few in number ($N_{10'-30'} = 24$) and those galaxies in the sample are bright, we use the stars to determine the PSF to use for comparison to this sample. The compact galaxies are generally distant ($\langle V_{rad} \rangle = 5789 \text{ km/s}$) and unresolved ($D_{25} \leq 1.5'$). These control galaxies are much more numerous ($N_{con} = 200$) than the stars, and have brightness characteristics that are very well matched to the two sets of sample galaxies, $2.5' - 5'$ and $5' - 10'$, to which they are compared. Figure 6 shows the distribution of recessional velocities, R_{25} , and M_B for the control galaxies. As is the case for the sample galaxies, the control galaxies are predominantly of types Sc and earlier (see Figure 5). This set of control objects results in a conservative estimate of the PSF because the dust emission from these galaxies is not necessarily unresolved. See Table 1 for a summary of the mean properties of the two control samples.

We calculate the PSF using these two control samples and Monte Carlo techniques to reproduce the range of spatial rescalings and rotations applied to the data. Our procedure includes:

- (1) the extraction of a $121.5' \times 121.5'$ control galaxy sub-image, randomly selected from the complete control set;
- (2) the control sub-image is spatially rescaled and rotated using parameters

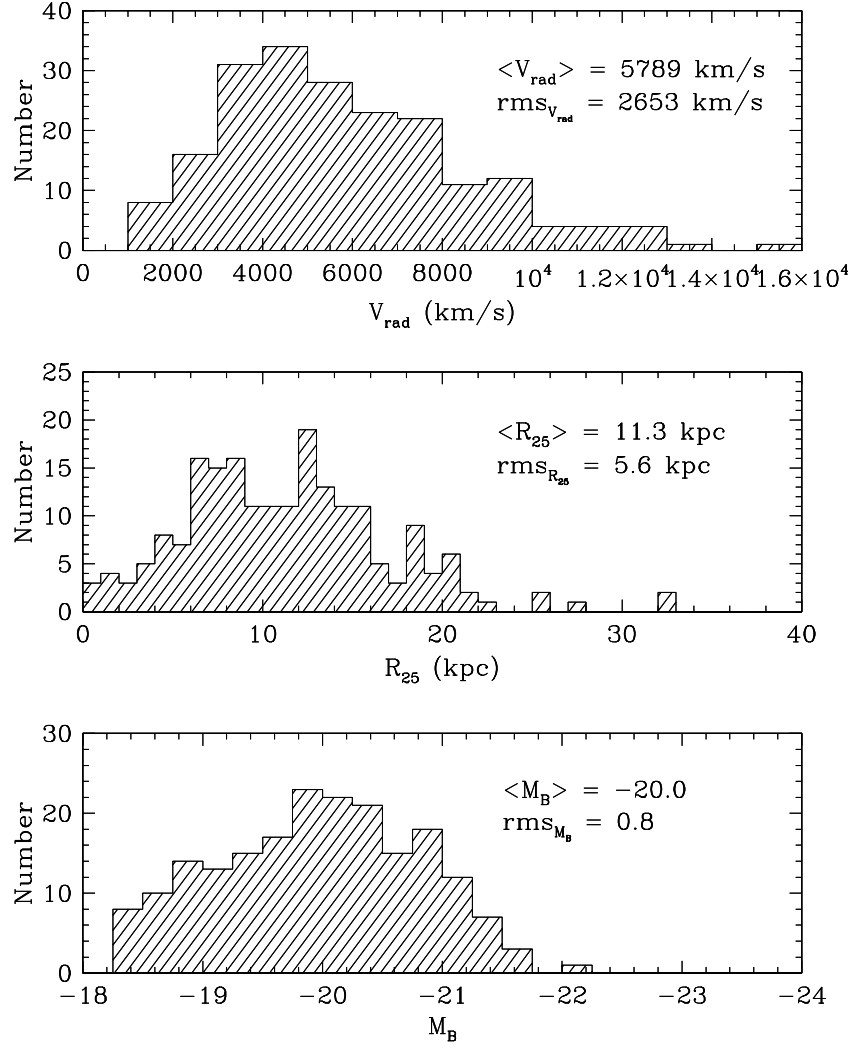


Fig. 6.— The distributions of recessional velocities, R_{25} , and M_B for the control sample of 200 galaxies.

drawn from a corresponding sample galaxy;

(3) the control galaxy is sky-subtracted and normalized so that its central surface brightness equals unity, as is done for the sample galaxies.

These steps are repeated until the number of randomly selected control galaxies equals the number of sample galaxies. The control objects are then coadded using the same algorithm as outlined previously for the sample galaxies to produce an image of the PSF. For the $2.5' - 5'$ and $5' - 10'$ samples, we repeat this procedure 20 times to get a mean representation of the point spread function and a measurement of the uncertainty in the mean PSF. For the $10' - 30'$ sample, the number of control stars is comparable to the number of sample galaxies and thus we only repeat the above Monte Carlo procedure 10 times to derive a corresponding mean PSF.

3. Results

Any $100\mu\text{m}$ flux in excess of that expected from a point source is a direct detection of extended emission from galaxies. To determine if excess emission exists, we construct residual images by subtracting the PSF image from the coadded sample image. The residual image for the $10' - 30'$ sample is presented in Figure 7, where the left hand and right hand panels are the residual images before and after rebinning into polar coordinates, respectively. The residual image was produced by combining the sample galaxy images using a median filter. The right hand panel shows $100\mu\text{m}$ emission that is easily visible to a radius of $\sim 1.1 R_{25} \simeq 21$ kpc. Also, both panels illustrate that the residual emission is most extended along the optical major axis of the disk, thus indicating that the dust responsible for the $100\mu\text{m}$ emission is flattened into a disk.

The radial distribution of the residual $100\mu\text{m}$ emission (averaged over $0^\circ \leq |\theta| \leq 22.5^\circ$, where θ is the angle such that 0° is along the disk major axis) for all three samples is shown in Figure 8. The mean PSF has been subtracted from the coadded sample galaxies (combined using a median filter) and also, for comparison, from each individual Monte Carlo realization of the control. Uncertainties in the residual surface brightness profile are calculated from the rms scatter of the various Monte Carlo realizations of the control samples. At the 2σ level, $100\mu\text{m}$ emission extends to a radius of $1.1R_{25} \simeq 21$ kpc for the $10' - 30'$ sample and to $1.2R_{25} \simeq 23$ kpc at the 1σ level (Fig 8, left panel). For the $5' - 10'$ sample, residual $100\mu\text{m}$ extended emission is detected to a radius of $1.5R_{25} \simeq 27$ kpc at the 2σ level and to $1.8R_{25} \simeq 33$ kpc at the 1σ level (Fig 8,

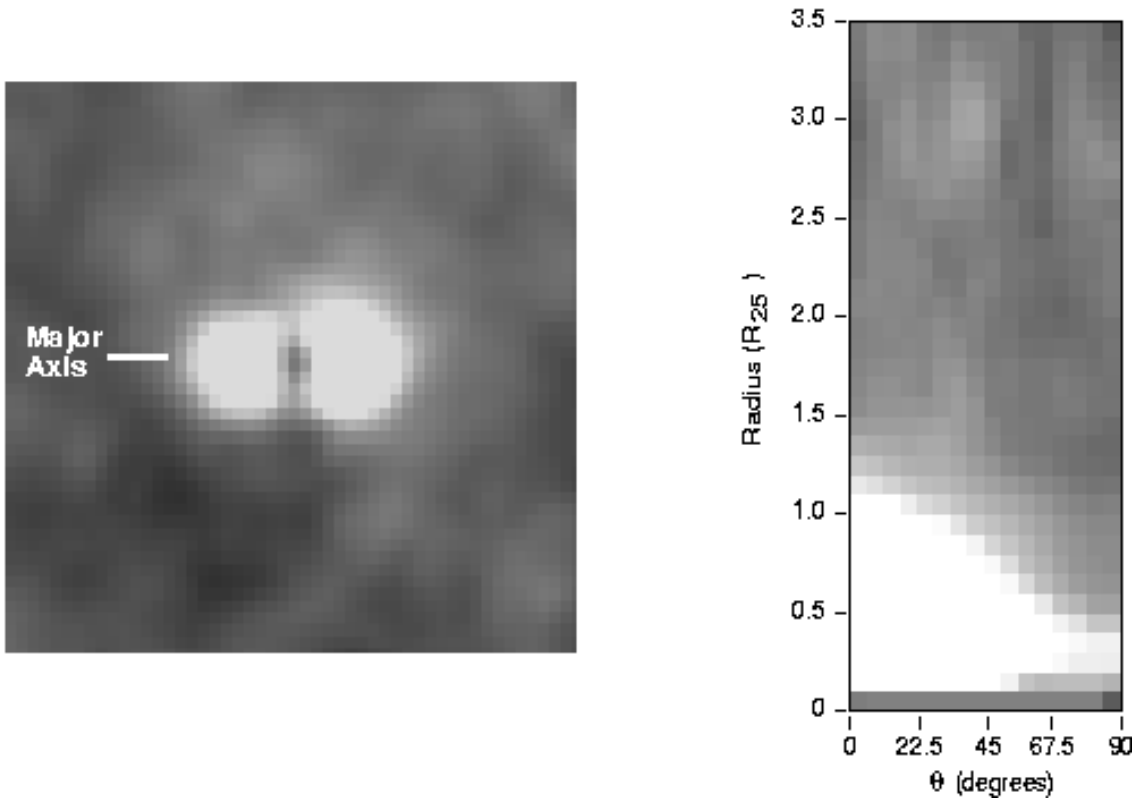


Fig. 7.— Residual images for the $10' - 30'$ sample, before (*left panel*) and after (*right panel*) rebinning into polar coordinates. The left panel image is $\sim 45' \times 45'$. The residual is determined by calculating the mean image of the 10 Monte Carlo realizations of the control PSF and subtracting the mean PSF from the coadded sample of galaxies image. Lighter shades correspond to higher flux. $100\mu\text{m}$ emission is visible to a radius of $\sim 1.1R_{25} \simeq 21$ kpc and is most extended along the major axis of the disk, demonstrating that $100\mu\text{m}$ emitting dust is flattened into a disk.

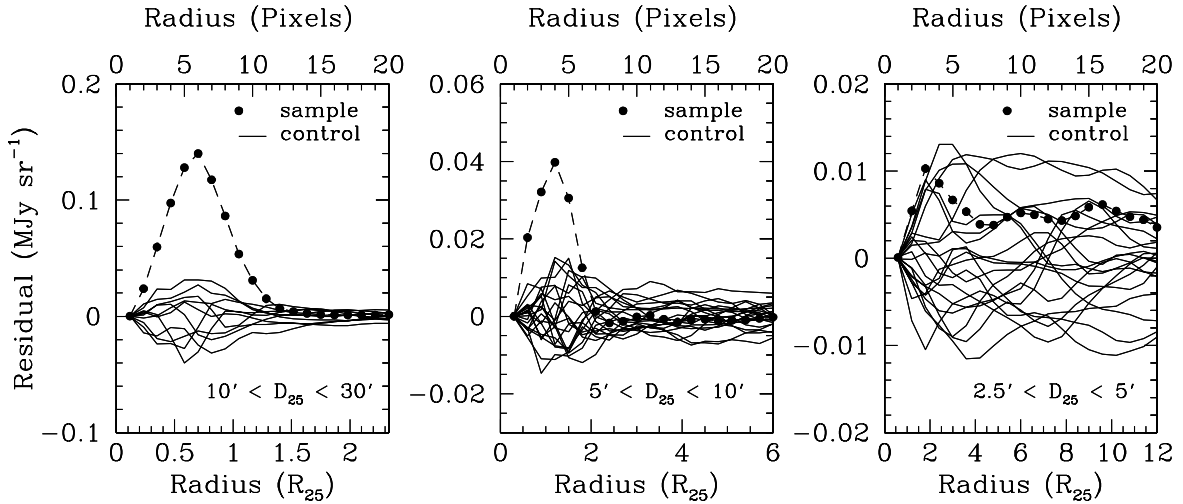


Fig. 8.— The surface brightness profile (averaged over $0^\circ \leq \theta \leq 22.5^\circ$, where θ is the azimuthal angle such that 0° is along the disk major axis) for the $10' - 30'$ sample (*left panel*), the $5' - 10'$ sample (*middle panel*), and the $2.5' - 5'$ sample (*right panel*). The mean PSF has been subtracted from the coadded sample galaxies and also from each individual Monte Carlo realization of the control. The scatter of the various realizations of the control residuals are indicative of the uncertainties and any emission above this scatter is a significant detection. Extended $100\mu\text{m}$ emission is seen to radii of $1.1R_{25} \sim 21$ kpc for the $10' - 30'$ sample and $1.5R_{25} \sim 27$ kpc for the $5' - 10'$ sample at the 2σ level.

middle panel). The $2.5' - 5'$ sample (Fig 8, right panel) shows no significant extended emission at any radii. This null detection is consistent with our two previous detections because the apparent angular size of the $100\mu\text{m}$ detection in the two nearby samples is not resolvable at the mean distance of the $2.5' - 5'$ sample and thus serves as a check on our method, demonstrating that a spurious detection is not produced by the method. These results are summarized in Table 2. Combination using an average filter produces virtually identical results (at the 2σ level: $1.1R_{25} \simeq 21$ kpc for the $10' - 30'$ sample and $1.8R_{25} \simeq 33$ kpc for the $5' - 10'$ sample) and therefore are not shown explicitly. Because the results are the same using either the average or median combination, we are assured that these detections are not due to one (or a few) dominant galaxies. Rather, extended $100\mu\text{m}$ emission is a typical feature of disk galaxies.

4. Discussion

We now investigate the distribution of the $100\mu\text{m}$ emission in more detail and attempt to constrain the distribution of dust. First, we examine the radial shape of the far-IR surface brightness profile and compare it to that of the underlying stellar component. Second, we use a simple model to convert the surface brightness profile to a dust mass profile. Finally, we briefly discuss the implications of our derived dust mass distribution.

4.1. $100\mu\text{m}$ Surface Brightness Profile

We have detected $100\mu\text{m}$ emission at radii of 21 kpc for the $10' - 30'$ sample and 27 kpc for the $5' - 10'$ sample at the 2σ level, but what is the shape of that surface brightness profile? Although the resolution of our data is coarse ($\text{HWHM}_{10'-30'} \simeq 9.5$ kpc and $\text{HWHM}_{5'-10'} \simeq 19$ kpc), the pixel scale (1.9 kpc pixel^{-1} for the $10' - 30'$ sample and 5.7 kpc pixel^{-1} for the $5' - 10'$ sample) is sufficiently small to provide for several pixels of coverage over the detection. We do not resolve extended emission along the disk minor axis and therefore, we confine ourselves to parametrizing the major axis profile. However, we can conclude that the $100\mu\text{m}$ emission is confined to within 9.5 kpc of the disk plane for the $10' - 30'$ sample and within 19 kpc for the $5' - 10'$ sample (independent of inclination because these are upper limits).

Along the direction of maximum emission ($0^\circ \leq |\theta| \leq 22.5^\circ$), we fit an exponential radial profile to the surface brightness, a model for the underlying light distribution, convolved with a Gaussian, a model for the PSF. Because

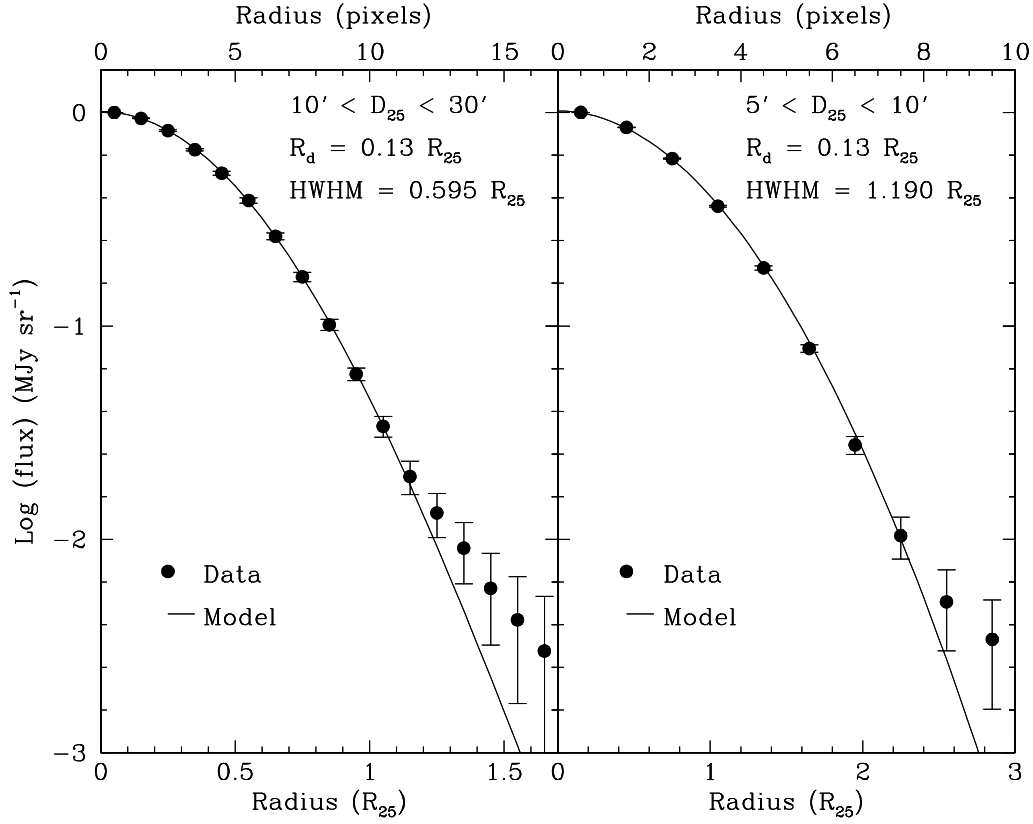


Fig. 9.— The simultaneous best fit to the $100\mu\text{m}$ surface brightness profiles of the $10' - 30'$ sample (*left panel*) and the $5' - 10'$ sample (*right panel*), before renormalizing the errors. The surface brightness profiles are modelled by an exponential convolved with a Gaussian (see text for details). The 1σ error bars plotted are derived from the rms scatter of the mean of the various Monte Carlo realizations of the control samples.

we do not know the effective PSF or the exponential scale length of the $100\mu\text{m}$ emission, both the HWHM of the Gaussian and the exponential scale length, r_d are free parameters. We simultaneously fit the data from both samples to the convolved function by minimizing χ^2 (and imposing the conditions that $\text{HWHM}_{5'-10'} = 2.0 \times \text{HWHM}_{10'-30'}$ and that the exponential scalelengths be the same). Figure 9 demonstrates our best fit, which is obtained for $\text{HWHM}_{10'-30'} = 0.595R_{25} = 11.0$ kpc and $r_d = 0.13R_{25} = 2.4$ kpc, with a reduced $\chi^2 = 2.84$. For the majority of the $100\mu\text{m}$ surface brightness profile, the best fit is generally within the 1σ error bars, which are derived from the rms scatter of the mean of the various Monte Carlo realizations of the control samples. More significant deviations occur in the outer regions of the profile, when the flux values approach sky levels ($\sim 1R_{25}$ for the $10' - 30'$ sample and $\sim 2R_{25}$ for the $5' - 10'$ sample). Although the errors are large, we may be seeing evidence for a second, more extended component at large radius ($r \gtrsim 25$ kpc).

The task of determining the uncertainties of the parameters is more difficult than that of identifying the best parameters. Although some parameters yield good fits that cannot be rejected at a confidence level $>90\%$, neither model has a reduced $\chi^2 \sim 1$. Either the model is not entirely representative and there is a nonexponential tail to the dust emission, or the uncertainties are underestimates. We conservatively suggest that χ^2 is inflated. As a result of details of the polar rebinning procedure, pixels at small radii are not independent (i.e. for small r , one (x, y) pixel contributes to different (r, θ) pixels after rebinning). Therefore, the calculated rms scatter for pixels at small r does not fully reflect the uncertainties. To compensate for this effect, we now renormalize the errors in the following manner. Because the underestimation of uncertainties is more severe at small radii than at large, we renormalize the errors using a factor $\propto A/r$ and define A to result in $\chi^2 = 1.0$ while fixing the model Gaussian to have $0.585R_{25} \leq \text{HWHM}_{10'-30'} \leq 0.595R_{25}$, drawn from the best fit (the IPAC estimated PSF has $\text{HWHM}_{10'-30'} \sim 0.50R_{25}$). Using the renormalized errors and fixing the range of the HWHM, we again simultaneously fit the models to the data from both samples and find the following parameter range acceptable within the 90% confidence level: $0.09R_{25} \leq r_d \leq 0.18R_{25}$ or $1.7 \text{ kpc} \leq r_d \leq 3.3 \text{ kpc}$.

One important result that may be casually overlooked is the significance of simultaneously fitting the data from both samples to the same exponential. One might naively expect that dust should be detected in either sample out to the same radius, particularly since, as pointed out previously, the galaxies in these two samples do appear to be the same type of galaxies ($\langle R_{25} \rangle \sim 18.5$ kpc

Table 2. $100\mu\text{m}$ Emission Detections

Sample	$100\mu\text{m}$ Emission Detection	
	2σ Detection	1σ Detection
$10' - 30'$	$1.1R_{25}$ 21 kpc	$1.2R_{25}$ 23 kpc
$5' - 10'$	$1.5R_{25}$ 27 kpc	$1.8R_{25}$ 33 kpc
$2.5' - 5'$	no emission detected	

Table 3. Best Fit^a Parameters for $100\mu\text{m}$ Surface Brightness Profile Fitting

Sample	$\text{HWHM}_{10'-30'}$	r_d
$10' - 30'$	$0.520R_{25} - 0.650R_{25}$ 9.6 kpc - 12.0 kpc	$0.05R_{25} - 0.20R_{25}$ 0.9 kpc - 3.7 kpc
$5' - 10'$	$0.565R_{25} - 0.610R_{25}$ 10.5 kpc - 11.3 kpc	$0.05R_{25} - 0.20R_{25}$ 0.9 kpc - 3.7 kpc
Simultaneous fits to both samples	$0.585R_{25} - 0.595R_{25}$ 10.8 kpc - 11.0 kpc	$0.09R_{25} - 0.18R_{25}$ 1.7 kpc - 3.3 kpc

^aWithin 90% confidence level

for both samples). However, due to the differences in sample size, the mean distance of galaxies in the two samples, and the effect of the PSF on samples of different angular size, the sensitivities are not the same. Separate fits to the two samples yield the 90% confidence parameter ranges given in Table 3. The range of acceptable parameter space allowed by fitting the two samples separately is consistent with that allowed by simultaneously fitting both samples and with each other.

How does our derived $100\mu\text{m}$ emission scalelength compare to that of the stellar component in a typical disk galaxy? The most recent and complete study of stellar disks is that of de Jong (1996a, 1996c), who uses near-infrared and optical broadband surface photometry of 86 face-on, disk dominated galaxies to investigate the distribution of disk and bulge parameters. Because K-band light is less affected by dust obscuration than B-band light, we choose to compare our result to the distribution of K scalelengths which range from $\sim 1 - 10$ kpc, with a median of $r_d^K = 3.8$ kpc, and a rms dispersion of 2.4 kpc (for $H_0 = 75$ km/s/Mpc). However, the distribution of scalelengths is a positive definite quantity with a significant high-end tail that is not described by a Gaussian. Therefore, the median is biased to a larger value than the peak of the distribution, which is quite broad and is in the range $\sim 2 - 4$ kpc (40% of the galaxies have scalelengths in this range). This range overlaps the 2.5 ± 0.8 kpc range of $100\mu\text{m}$ scale lengths that we measure. Because de Jong finds no correlation of scalelength with galaxy type, any differences in the distribution of galaxy type between the optical study and our samples is unimportant. We conclude that the derived $100\mu\text{m}$ scalelength is most likely not much larger than that of the underlying old stellar component and is consistent with being equivalent to or up to a factor of two smaller than that of the stellar distribution.

4.2. A Simple Model for the Dust Distribution

The characteristic scale length of the $100\mu\text{m}$ emission derived in the previous section can be used, in conjunction with simple modelling, to place a limit on the global dust mass distribution. Because we have data in a single passband with poor spatial resolution, we follow the procedure of Bothun & Rogers (1992), who use a one-component model (a single blackbody with characteristic temperature) to describe the far-IR emission from dust, based on $60\mu\text{m}$ and $100\mu\text{m}$ IRAS images. The one-component assumption is questionable because of different temperature dust components needed to fit observed far-IR spectral energy distributions. Some find that multi-component models are needed to

explain their far-IR observations (e.g. Helou 1986; Rowan-Robinson & Crawford 1989; Andreani & Franceschini 1996), while others concur with Bothun & Rogers (1992) and find that their far-IR spectra can be well fit by a single component model (e.g. Sodroski *et al.* 1994; Clements, Andreani and Chase 1993; Odenwald, Newmark and Smoot 1996). Using DIRBE all-sky data, Sodroski *et al.* (1994) showed that a ubiquitous far-IR component can be detected as a single component at $60\mu m < \lambda < 240\mu m$ with $17K < T_d < 22K$ that is closely associated with the far-IR cirrus discovered by IRAS at $100\mu m$. Studies of IR selected galaxies find that the galaxies' continua are consistent with a single component model with $25 \lesssim T_d \lesssim 35$, and a peak emission near $100\mu m$ (Clements, Andreani and Chase 1993; Odenwald, Newmark and Smoot 1996). While dust certainly exists at a variety of temperatures, we use a simple one component model because of the limited temperature information provided by our single band data, and the evidence that the far-IR continua of the $100\mu m$ emitting dust is well fit by a single temperature blackbody in the range $20\text{ K} \lesssim T_d \lesssim 35\text{ K}$. Subsequent observations at mm wavelengths will be necessary to test this assumption.

Bothun & Rogers (1992) model the $100\mu m$ emission using an isothermal dust slab at a dust temperature, T_d , that is optically thin to far IR emission. They assume that within each region of the disk sampled by a pixel, radiative equilibrium exists between the interstellar radiation field (ISRF) and the dust grains, and also that the ISRF, represented by mean intensity, J_ν , is uniform over the region. They derive the following relationship between f_{ν_0} , the observed flux density in an IRAS passband with effective frequency ν_0 , and the integrated mean intensity J :

$$f_{\nu_0} \propto \mathcal{F}_{\nu_0}(T_d)\tau_J J, \quad (1)$$

where τ_J is the mean-intensity-weighted optical depth of the dust and \mathcal{F}_{ν_0} is the fraction of the total emission contained within the IRAS band. For a power law dust emissivity law that is proportional to ν^p , \mathcal{F}_{ν_0} can be expressed as

$$\mathcal{F}_{\nu_0} = \int_0^\infty \frac{x^{3+p}}{e^x - 1} R_x dx / [\Gamma(4+p)\zeta(4+p)], \quad (2)$$

where $x = h\nu/kT_d$, R_x is the system response for the band that is tabulated in the IRAS Explanatory Supplement, and Γ and ζ are the Gamma and Riemann Zeta functions.

Because τ is proportional to mass in the optically thin regime, we can use the above equations to trace dust mass as a function of radius if we know the dust temperature profile, the $100\mu m$ light profile, and the integrated mean

intensity profile of the ISRF. The radial profile of the dust mass distribution can be derived without needing to derive the various coefficients which are difficult to determine empirically. We assume that

$$J \propto \exp(-r/r_s), \quad (3)$$

where r is the radius and r_s is the scale length of the stellar component. In the previous section, we determined that the $100\mu\text{m}$ emission is also described by an exponential and thus

$$f_{\nu_0} \propto \exp(-r/r_d), \quad (4)$$

where r_d is the $100\mu\text{m}$ emission scale length. The only term in these equations that depends on the dust temperature is \mathcal{F}_{ν_0} . Bothun & Rogers (1992) using $60\mu\text{m}$ and $100\mu\text{m}$ images for 28 nearby galaxies, found that the dust temperature declines radially, due to the exponentially declining ISRF. These authors modeled the temperature profile with an exponential

$$T_d \propto \exp(-r/r_d), \quad (5)$$

which, for a limited range of scalelengths, can be approximated by a drop of 3 K for every optical scale length (Bothun & Rogers 1992). This temperature profile is consistent with their data out to a radius of ~ 3 optical scalelengths, where the temperatures converge to a near constant value of ~ 28 K (Bothun & Rogers). Therefore, we use the exponential temperature gradient, normalized to produce $T_d = 34.9$ K at one optical scale length and converging to a constant temperature of 28 K for $r > 3r_s$.

We can now solve for the dust distribution once we adopt values for the $100\mu\text{m}$ emission scale length, r_d , and the scalelength of the stellar component, r_s . For r_d , we choose the mean of the two best fit values, $r_d = 2.5$ kpc. As discussed previously, the $100\mu\text{m}$ scalelength could be equal or up to a factor of ~ 2 smaller than the stellar scalelength. Thus, we investigate the regime $0.5 \leq r_d/r_s \leq 1$. When $r_d/r_s = 1$, the model predicts a slight fall in the dust mass distribution in the inner regions of the galaxy (due to the radial temperature gradient) and then the dust mass distribution flattens out when the temperature converges to a constant. In the absence of a temperature gradient, the distribution is flat at all radii. This result occurs because Eq. 1 simplifies to $\tau \propto 1/\mathcal{F}_{\nu_0}(T_d)$, for equal stellar and dust emission scalelengths. If the temperature is constant with radius, then \mathcal{F}_{ν_0} is constant, and τ is independent of radius. For $0.5 \leq r_d/r_s < 1$, an exponentially declining dust mass with radius is predicted, with the dust being less centrally concentrated than the stars. As r_d/r_s decreases, the dust

mass scalelength decreases until it equals the stellar emission scalelength for $r_d/r_s = 0.5$.

A flat or slowly declining exponential radial dust distribution is consistent with the findings from optical studies. de Jong (1996b) studied the optical and infrared color profiles of 86 face-on disk-dominated galaxies using models of well mixed stars and dust that include both scattering and absorption. He found that high central optical depths and long dust scalelengths best reproduced the observed color gradients. However, he cautions that a realistic dust distribution alone cannot adequately account for the observed gradients, and that stellar population characteristics, namely age and metallicity gradients, need to be incorporated. Peletier *et al.* (1995) also studied spiral galaxies in the optical and infrared using models of smoothly distributed dust and stars that only included absorption, but also concluded that $r_d/r_s > 1$. However, when they included scattering and clumpiness in the dust models, $r_d/r_s \geq 1$ yielded acceptable solutions.

4.3. Implications of the Dust Mass Distribution

How does the dust distribution compare to other galaxy components? Neutral hydrogen has a radially flat distribution (Shaya & Federman 1987), while molecular gas appears to decline exponentially (e.g. Young & Scoville 1991). Because our data cannot distinguish between a flat or exponentially declining distribution of dust, we will discuss both cases. Some authors find a good correlation between FIR luminosities and the distribution of molecular gas (e.g. Devereux & Young 1990a, 1990b, 1992, & 1993, Tinney *et al.* 1990, Sanders *et al.* 1991, Downes *et al.* 1993, Sage 1993). Devereux & Young (1990a, 1990b, 1992, & 1993) studied the origin of the FIR luminosity in IR luminous spiral galaxies and concluded that FIR luminosity is an excellent indicator of star formation, being well correlated with $H\alpha$ luminosity and the surface density of H_2 (as inferred from CO observations) and poorly correlated with the surface density of HI. These authors claim that their observed FIR luminosities are due to the reradiation by warm dust of UV flux from young OB stars in HII regions, and therefore, the dust exponentially declines with radius as do the stellar and molecular components.

Others provide evidence for a second cooler, more diffuse cirrus-type component, that is associated with the HI rather than star forming regions and excited by the ISRF from old disk stars. Using a model that includes both components, Lonsdale-Persson & Helou (1987) have calculated that cirrus-type

emission can account for up to between 50% and 70% of the total FIR emission from a median spiral galaxy, and subsequent observations have supported their claim (Walterbos & Schwering 1987, Rice *et al.* 1990, Sauvage & Thuan 1992, Xu & Helou 1996). Furthermore, Sauvage & Thuan (1992) observationally determined that the fractional contribution of cirrus-type emission to the total FIR of spiral galaxies is a function of type: $\sim 3\%$ for Sdm, increasing to $\sim 70\%$ for Sc galaxies, and reaching as high as $\sim 86\%$ for Sa galaxies. When normal spiral galaxies (i.e. not ultra luminous IRAS galaxies nor active galaxies) are studied, the contribution from the cirrus component becomes important and non-negligible correlations between cold dust and HI are found, although cold dust is better correlated with the total gas content (HI + H₂) than with either phase separately (e.g. Knapp, Helou, & Stark 1987, Andreani, Casoli, & Gerin 1995, Xu & Helou 1996). Xu & Helou (1996) studied the diffuse component of the FIR emission of M31 by removing FIR emission associated with HII regions and found a close association of the diffuse cirrus-type component with HI, while a poor correlation was found with H₂. Interestingly, these authors calculate the radial behavior of the V-band optical depth, τ_V , and find that the overall distribution of τ_V is rather flat out to a radius of ~ 14 kpc.

Because the galaxies in our samples are predominantly of type Sc and earlier, we expect the cirrus component, rather than the dust component associated with HII regions, to be the main contributor to the FIR emission. However, a number of authors have demonstrated that IRAS is not very sensitive to emission by cold dust and that the emission from large amounts of cold dust can easily be dominated by emission from a small amount of warm dust (e.g. Bothun & Rogers 1992, Sage 1993, Block *et al.* 1994). In reality, the 100 μ m emitting dust detected in our sample is probably associated, at some level, with both the molecular and atomic gas phases. While our assumed dust temperature of ~ 30 K is similar to dust temperatures derived for samples of nearby spirals (e.g. Young *et al.* 1986, Walterbos & Schwering 1987, Jura 1986, Bothun & Rogers 1992), this is not the characteristic temperature of either HII regions, which are hotter, nor the HI interstellar medium, which is typically colder. Our assumed dust temperature was derived by Bothun & Rogers (1992) using a single temperature model, based on 60 μ m and 100 μ m data with very coarse resolution where each pixel samples a wide range of local heating conditions, and consequently is probably an average of the temperatures of the two contributing components. Therefore, although our data do not allow us to differentiate between a flat and exponentially declining distribution of dust, the 100 μ m emission measured in our sample almost assuredly originates from both warm dust residing in HII

regions and associated with the exponentially declining molecular gas and also from the cooler, cirrus component associated with the flatly distributed neutral hydrogen .

Ultimately, we would like to know the radial extent of the dust layer. In particular, does it have a cutoff at some radius? Unfortunately, our current data do not allow us to answer this question, but we can use them to place a lower limit on that cutoff radius. We have detected $100\mu\text{m}$ emission from dust out to a radius of 27 kpc (with $\geq 2\sigma$ confidence). This is a lower limit to the cutoff radius and large amounts of cold dust at larger radii could exist. We can compare this limit to the known edges of the stellar (e.g. van der Kruit & Searle 1981a, 1981b, 1982a, 1982b) and neutral hydrogen (e.g. Corbelli, Schneider & Salpeter 1989, Corbelli & Salpeter 1993, Bland-Hawthorn, Freeman & Quinn 1997) disks. van der Kruit *et al.* (1982a) found that all of the stellar disks in their sample of 8 galaxies have a sharp edge at 4 - 5 radial scalelengths, or 14 - 25 kpc with an average value of 17 kpc. Neutral hydrogen disks also have a sharp boundary, although at radii beyond the edge of the stellar disk. For example, galaxies in the Sculptor group have observed HI disks that extend to $\sim 1.2R_{25} \sim 23$ kpc (Bland-Hawthorn, Freeman & Quinn 1997). Few galaxies have HI disks that extend farther to $\sim 2R_{25} \sim 38$ kpc (Bland-Hawthorn, Veilleux & Carignan 1997, Bland-Hawthorn, Freeman & Quinn 1997). The radial edge of our $100\mu\text{m}$ detection, at a radius of 27 kpc, is beyond 4 - 5 stellar scalelengths and therefore, beyond the edge of the stellar disk. We do not observe far-IR emission beyond the nominal edge of HI disks, although because our detection is a lower limit, dust may extend beyond the edge of the HI disk.

If dust is produced by stars, how can dust be found outside the stellar disk? One can speculate that it is primordial, i.e. that it formed early in the process of galaxy formation and then settled into a disk similarly to the HI, that galactic fountains, plumes of gas and dust ejected by supernovae into the interstellar medium, pollute the outer galaxy, or that some disk stars exist at these large radii. Models of galactic fountains (e.g. Corbelli & Salpeter 1988) show that some of the hot material ejected by violent supernovae, can rise many kiloparsecs into the halo and then radiatively cool and fall back toward the outer part of the galactic plane at distances ≥ 20 kpc. A similar, but less energetic mechanism of ejecting dust into the ISM involves radiation pressure produced by clusters of young OB stars. Models of these dusty chimneys by Ferrara (1995) show that some dust particles can attain rather high velocities (~ 100 km/s) and reach distances of ~ 3 kpc above the disk plane. However, the majority of the dust particles' motion is in a direction perpendicular, rather than parallel, to

the plane of the disk. The redistribution of dust particles’ in Ferrara’s models predicts a flattened dust distribution, which is consistent with our work (see Fig 7). Lastly, although stellar disks are observed to truncate sharply, there is observational evidence for massive star formation in the outer regions of galactic disks. Hodge *et al.* (1988) and Davidge (1993) found blue stars in two different fields in the outer disk (~ 20 kpc) of M31. If these findings are representative of spiral galaxies, then there is at least some star formation at the very edge of stellar disks which could contribute dust at large radii. Therefore, there are several avenues that need to be more fully explored to determine the mechanism involved in getting dust to $r \sim 30$ kpc.

5. Summary

Using $100\mu\text{m}$ ISSA images and data from the RC3, we coadd the flux from 299 galaxies and investigate the radial and azimuthal distribution of $100\mu\text{m}$ emission from dust in ensembles of galaxies. The galaxies are divided into three samples (where N = number of galaxies), according to their optical isophotal diameter, D_{25} : (1) $2.5' \leq D_{25} \leq 5.0'$ ($N_{2.5'-5'} = 184$), (2) $5.0' \leq D_{25} \leq 10.0'$ ($N_{5'-10'} = 91$), and (3) $10.0' \leq D_{25} \leq 30.0'$ ($N_{10'-30'} = 24$). We find the following:

- (1) that $100\mu\text{m}$ emission extends out to radii of 27 kpc at the 2σ or greater confidence level for the $5' - 10'$ sample and to 21 kpc for the $10' - 30'$ sample (no extended emission is seen beyond the PSF for the $2.5' - 5'$ sample),
- (2) that the $100\mu\text{m}$ emission from both the $5' - 10'$ and $10' - 30'$ sample is preferentially elongated along the major axis of the disk, thus confirming the validity of the detections and demonstrating that $100\mu\text{m}$ emitting dust is flattened into the disk,
- (3) that the $100\mu\text{m}$ surface brightness profiles from both samples can be well fit with an exponential with a dust emission scale length of $\sim 2.5 \pm 0.8$ kpc, but there is evidence for a second, more extended emission component, and
- (4) that a model of the $100\mu\text{m}$ emission from an isothermal dust slab at temperature, T_d , that is optically thin to emission can be used to model our data (cf. Bothun & Rogers 1992). Because our data do not allow us to calculate dust temperatures, we adopt the dust temperature gradient derived by Bothun & Rogers (1992), which can be approximated by a drop of 3 K for every optical scale length, r_s , and is normalized by $T_d = 34.9$ K at one optical scale length and converges to a near constant value of ~ 28 K for $r > 3r_s$. Using this model, we examine the range of acceptable dust mass distributions allowed by our data

and find that the dust is less concentrated than the stars, with either a flat or slowly declining exponential distribution.

We have presented evidence for dust well beyond the stellar disk, but have been unable to conclude whether dust exists beyond the extent of the HI distribution. Such dust, if present, should be quite cold ($\lesssim 10$ K) and difficult to detect with IRAS observations, despite the possible evidence of a second component in our data. The future of this field relies on longer wavelength observations. Preliminary detections of dust at large radii using $200\mu\text{m}$ observations have recently been presented by Alton *et al.* (1998). We await further results from such observations.

Acknowledgments: DZ acknowledges funding from a NASA LTSA grant (NAG-5-3501), a NSF grant (AST-9619596), and the Packard Foundation. AEN & DZ gratefully acknowledge financial support from the Cal Space Foundation. AEN gratefully acknowledges financial support from the University of California Graduate Research Mentorship Fellowship program. RMC acknowledges the support of the Jet Propulsion Laboratory, Caltech, which is operated under contract with NASA.

References

- Alton, P.B., Davies, J.I., Bianchi, S. & Irewhella, M. 1998 in “Galactic Halo: A UC Santa Cruz Workshop”, D. Zaritsky (ed.), (San Francisco: ASP), p.149
- Andreani, P., Casoli, F. & Gerin, M. 1995, AA, 1995, 43
- Andreani, P., & Franceschini, A. 1996, M.N.R.A.S., 283, 85
- Bland-Hawthorn, J., Freeman, K.C. & Quinn, P.J. 1997, ApJ, 490, 143
- Bland-Hawthorn, J., Veilleux, S., & Carignan, C. 1997, in prep.
- Block, D., Witt, A., Grosbol, P., Stockton, A., Moneti, A. 1994, AA, 288, 383
- Bothun, G.D., Lonsdale, C.J., & Rice, W. 1989, ApJ, 341, 129
- Bothun, G.D., & Rogers, C. 1992, AJ, 103, 1484
- Clements, D.L., Andreani, P. & Chase, S.T. 1993, M.N.R.A.S., 261, 299
- Corbelli, E. & Salpeter, E.E. 1988, ApJ, 326, 551
- Corbelli, E. & Salpeter, E.E. 1993, ApJ, 419, 104
- Corbelli, E., Schneider, S.E. & Salpeter, E.E. 1989, AJ, 97, 390
- Davidge, T.J. 1993, ApJ, 409, 190
- Devereux, N.A. & Young, J.S. 1990a, ApJL, 350, L25
- Devereux, N.A. & Young, J.S. 1990b, ApJ, 359, 42
- Devereux, N.A. & Young, J.S. 1992, ApJ, 103, 1536
- Devereux, N.A. & Young, J.S. 1993, ApJ, 106, 949
- Downes, D., Solomon, P., Radford, S. 1993, ApJL, 414, L13
- Fall, S.M. & Efstathiou, G. 1980, M.N.R.A.S., 193, 189
- Ferrara, A. 1995 in “The Physics of Galactic Halos”, 156 WE-Heraeus-Seminar, H. Lesch *et al.* (eds.), (Verlag:Berlin)
- Fich, M., Blitz, L., Stark, A.A. 1989, ApJ, 342, 272
- Helou, G. 1986, ApJL, 311, L33
- Hodge, P., Lee, M.G., Mateo, M. 1988, ApJ, 324, 172
- de Jong, R.S. 1996a, AA, 313, 45
- de Jong, R.S. 1996b, AA, 313, 377
- de Jong, R.S. 1996c, AA, 313, 557
- Jura, M. 1986, ApJ, 306, 483
- Kennicutt, R.C. 1989, ApJ, 344, 685

- Knapp, G.R., Helou, G., & Stark, A.A. 1987, *ApJ*, 94, 54
- van der Kruit, P.C., & Searle, L. 1981a, *AA*, 95, 105
- van der Kruit, P.C., & Searle, L. 1981b, *AA*, 95, 116
- van der Kruit, P.C., & Searle, L. 1982a, *AA*, 110, 61
- van der Kruit, P.C., & Searle, L. 1982b, *AA*, 110, 79
- Lequeux, J., Allen, R.J., Guilloteau, S. 1993, *AA*, 280L, L23
- Lin, D.N.C., & Pringle, J.E. 1987, *ApJL*, 320, L87
- Lonsdale-Persson, C.J. & Helou, G. 1987, *ApJ*, 314, 513
- Low, F.J., *et al.* 1984, *ApJL*, 278, L19
- Maloney, P. 1993, *ApJ*, 414, 41
- Odenwald, S., Newmark, J. & Smoot, G. 1996 preprint (astro-ph/9610238)
- Peletier, R.F., Valentijn, E.A., Moorwood, A.F.M., Freudling, W., Knapen, J.H., & Beckman, J.E. 1995, *AA*, 300, L1
- Rice, W. 1993, *ApJ*, 105, 67
- Rice, W., Boulanger, F., Viallefond, F., Soifer, B.T. & Freedman, W.L. 1990, *ApJ*, 358, 418
- Rice, W., Lonsdale, C.J., Soifer, B.T., Neugebauer, G., Kopan, E.L. *et al* 1988, *ApJS* 68, 91
- Rowan-Robinson, M., & Crawford, J. 1989, *M.N.R.A.S.*, 238, 523
- Sage, L.J. 1993, *AA*, 272, 123
- Sanders, D.B., Scoville, N.Z., & Soifer, B.T. 1991, *ApJ*, 370, 158
- Sauvage, M. & Thuan, T.X. 1992, *ApJL*, 396, L69
- Shaya, E., & Federman, S. 1987, *ApJ*, 319, 76
- Sodroski, T. *et al.* 1994, *ApJ*, 428, 638
- Tinney, C.G., Scoville, N.Z., Sanders, D.B., & Soifer, B.T. 1990, *ApJ*, 362, 473
- de Vaucouleurs, G., de Vaucouleurs, A., Corwin, H.G., Buta, R.J., Paturel, G., & Fouque, P. 1991, *Third Reference Catalog of Bright Galaxies* (Springer, Berlin) (RC3)
- Walterbos, R.A.M. & Schwering, P.B.W. 1987, *AA*, 180, 27
- Wheelock *et al.* 1994, *IRAS Sky Survey Atlas Explanatory Supplement*, JPL Publication 94-11.
- Wouterloot, J.G.A., Brand, J., Burton, W.B., Kwee, K.K. 1990, *AA*, 230, 21

Xu, C. & Helou, G. 1996, ApJ, 456, 163

Young, J.S., Schloerb, F.P., Kenney, J.P., & Lord, S.D. 1986, ApJ, 304, 443

Young, J.S., Scoville, N.Z. 1991, Ann. Rev., 29, 581

Zaritsky, D. 1994, AJ, 108, 1619